Integrated heterodyne laser Doppler vibrometer based on stress-optic frequency shift in silicon nitride

Adam Raptakis[1][*], Lefteris Gounaridis[1], Jörn P. Epping[2], Thi Lan Anh Tran[2], Thomas Aukes[3], Moritz Kleinert[4], Madeleine Weigel[4], Marco Wolfer[5], Alexander Draebenstedt[5], Christos Tsokos[1], Panos Groumas[1,6], Efstathios Andrianopoulos[1], Nikos Lyras[1], Dimitrios Nikolaidis[1], Elias Mylonas[1], Nikolaos Baxevanakis[6], Roberto Pessina[7], Erik Schreuder[2], Matthijn Dekkers[3], Volker Seyfried[5], Norbert Keil[4], René G. Heideman[2], Hercules Avramopoulos[1] and Christos Kouloumentas[1,6]

*Correspondence:
arap@mail.ntua.gr

[1] Photonic Communications
Research Laboratory,
Institute of Communication
and Computer Systems, National
Technical University of Athens,
15573 Zografou, Greece
[2] LioniX International BV, P.O.
Box 456, 7500 AL Enschede, The
Netherlands
[3] SolMateS BV, Auke Vleerstraat
3, 7521 PE Enschede, The
Netherlands
[4] Fraunhofer Institute
for Telecommunications, HHI,
1058 Berlin, Germany
[5] Polytec GmbH,
76337 Waldbronn, Germany
[6] Optagon Photonics, Agia
Paraskevi 15341, Athens, Greece
[7] Cordon Electronics Italia
S.R.L, San Martino 7, Agrate
Brianza 20864, Italy

Abstract

We demonstrate a compact heterodyne Laser Doppler Vibrometer (LDV) based on the realization of optical frequency shift in the silicon nitride photonic integration platform (TriPleX). We theoretically study, and experimentally evaluate two different photonic integrated optical frequency shifters (OFSs), utilizing serrodyne and single-sideband (SSB) modulation. Both OFSs employ stress-optic modulators (SOMs) based on the non-resonant piezoelectrical actuation of lead zirconate titanate (PZT) thin-films, deposited on top of the silicon nitride waveguides with a wafer-scale process. To improve the modulation bandwidth of the SOMs we investigate a novel configuration of the electrodes used for the actuation, where both electrodes are placed on top of the PZT layer. Using this top-top electrode configuration we report frequency shift of 100 kHz and 2.5 MHz, and suppression ratio of the unwanted sidebands of 22.1 dB and 39 dB, using the serrodyne and the SSB OFS, respectively. The best performing SOM structure induces 0.25π peak-to-peak sinusoidal phase-shift with 156 mW power dissipation at 2.5 MHz. We use the SSB-OFS in our compact LDV system to demonstrate vibration measurements in the kHz regime. The system comprises a dual-polarization coherent detector built in the PolyBoard platform, utilizing hybrid integration of InP photodiodes (PDs). High quality LDV performance with measurement of vibration frequencies up to several hundreds of kHz and displacement resolution of 10 pm are supported with our system.

Keywords: Photonic integration, Optical frequency shift, Stress-optic, PZT, Silicon nitride, Heterodyne interferometry, Laser doppler vibrometry

Introduction

Optical frequency shift (OFS) is a key function for the operation of sensing systems based on heterodyne interferometry, including distance metrology, laser Doppler velocimetry and vibrometry, or light detection and ranging (LIDAR) [1–3]. Today these systems are mostly large, since they still rely on free-space optical components. Their OFS unit in particular is typically based on bulky acousto-optic modulators that offer high conversion efficiency and low-noise operation, but they exhibit low flexibility in the selection of the frequency shift and require precise beam alignment at their input optical port [4, 5].

Efforts over the past years to miniaturize those sensing systems by means of photonic integration have resulted in waveguide-integrated implementations of their OFS unit based either on serrodyne modulation in a single-phase shifter [6–8] or on single-sideband (SSB) modulation in a quad array of phase shifters inside an in-phase/quadrature modulator (IQM) [9]. In [7, 8] the corresponding implementations were based on serrodyne modulation using thermal phase shifters in a silicon-on-insulator (SOI) platform, enabling the miniaturization of a LDV, which is a prominent example of heterodyne sensors [10]. Despite their importance from the miniaturization point of view, the low bandwidth of the thermal phase shifters in those works (which is by nature in the kHz regime) limits their applicability to only a short range of LDV applications.

At the higher end of the efforts for photonic integration of OFS units, the main work so far has involved the use of electro-optic phase shifters inside IQMs to perform SSB modulation. Many implementations have been originally concentrated in $LiNbO_3$ [11–13] due to its good electro-optical properties, but the emergence of silicon photonics in the more recent years, with the potential for large-scale integration, has motivated realizations also in silicon photonics [9, 14–16], including the silicon organic hybrid (SOH) platform [17]. Although broadband enough to enable spectral shifts in the GHz regime, those phase shifters can have a complex fabrication process, and can exhibit unwanted amplitude modulation in parallel with the target phase modulation. Via this mechanism, they can reduce in turn the side-mode suppression ratio (SMSR) of the original carrier and the spurious side modes with respect to the shifted spectral line, resulting in substantial degradation of the overall heterodyne detection [18]. In order to remove this amplitude modulation, SOH phase shifters can replace the pure silicon ones at the expense of additional complexity and cost in the fabrication process [17]. Alternatively, a pair of modulators inside an MZI switch has been proposed in [19] for improving the SMSR performance with conventional silicon modulators, but fast switching and precise synchronization between the modulators is required. A more direct approach to improve the SMSR in SSB modulation is to use driving signals with higher harmonics that can suppress the nonlinearity of the MZM inside the IQM [17, 20], but these techniques require driving electronics with significant larger bandwidth.

In the case of heterodyne sensors [6–9, 21], wherein the target OFS remains in the MHz regime, the development of a photonic integrated phase shifter technology that can fill the gap between the thermal phase shifters (operating in the kHz regime) and the electro-optic phase shifters (operating in the GHz regime) is a milestone, as it can offer beneficial tradeoffs in terms of bandwidth, cost and integration scale. Relevant efforts

have primarily involved the development of phase shifters based on strain-induced geometrical deformations of the modal cross-sections of waveguides in SOI or in silicon nitride. In [22] a comb-drive actuator in the form of a complex micro-electro-mechanical system (MEMS) was integrated in SOI to induce the deformation of a suspended silicon waveguide with operation bandwidth close to 1 MHz. Similar tuning speeds, but with piezoelectrical actuation of lead zirconate titanate (PZT) films, have been reported with a suspended ring resonator in silicon nitride [23].

A slightly different approach is the use of mechanical strain to change the refractive index of the waveguides [24]. Initial demonstrations of the stress-optic effect included dynamic control of the refractive index or the birefringence of silica [25] or silicon waveguides [26–28]. To our specific interest in the present work, PZT films were used to apply stress-optic index modulation in the silicon nitride platform called TriPleX [29–32]. Each PZT film was integrated on the surface of the TriPleX platform and in very close proximity to the corresponding waveguide, allowing for a non-resonant piezo-actuation of the mechanical strain. Non-resonant stress-optic modulation in the silicon nitride platform has also been demonstrated by LETI in [33]. Despite the theoretical potential of the PZTs for operation at 10 s or even 100 s of MHz, the demonstrated modulation speed of the PZT-based phase shifters in those works was kept in the kHz regime since the focus of the investigations was on the basic characterization of the phase shifters and the minimization of their power consumption in quasi-static operation. Modulation in the MHz regime based on the stress-optic effect has been recently demonstrated in silicon nitride using piezo-electric actuation of a micro-ring modulator [34]. A theoretical analysis for silicon nitride platforms and an early experimental work in a SOI platform were presented in [35] and [36] respectively, highlighting the potential for resonant creation of strain and deformation of the modal cross-section of waveguides via Rayleigh surface acoustic waves (SAWs). Excitation of SAWs has been previously relied in the good acousto-optical properties of $LiNbO_3$ to realize a heterodyne interferometer [21]. In [35] and [36] the SAW excitation was based on the use of PZT films on the surface of the platform and the use of inter-digital transducers (IDTs) instead of simple electrodes for the resonant actuation of those films. The potential operation speed of the phase shifters was deeply in the MHz regime, but at certain frequencies that could match the periodicity of the IDT structures.

Typically, light modulation in TriPleX relies on thermo-optic phase shifters, that are limited to modulation speeds of a few kHz. In cases where larger modulation bandwidth is needed, high-speed electro-optic modulators in Indium Phosphide (InP) are used (https://www.lionix-international.com/forms/triplex-silicon-nitride-whitepaper/), [37]. Although these modulators can offer bandwidth of several GHz, hybrid integration is used to combine them with the TriPleX platform, which increases the cost and complexity of the assembly, as the PICs must be diced and coupled together optically, rendering the process unsuitable for high-volume manufacturing (HVM). Deposition of PZT on the other hand, as well as the structuring of the stress-optic modulators (SOMs), is a wafer-level process that can be scaled for HVM [38, 39] and has the potential for significant cost-reduction in applications where modulation in the MHz regime is sufficient. Eliminating the need for hybrid integration in such applications has the obvious benefit of reducing the overall size of the PIC assembly, as well as the number of coupling

interfaces, and thus, minimizing the optical loss. On top of that, the SOM introduces minimal loss, since the PZT thin films are placed a few microns above the TriPleX waveguiding structures, leaving the propagating mode undisturbed.

In the present paper, we make a breakthrough in the work on non-resonant PZT phase shifters by demonstrating for the first time to our knowledge the operation potential of the PZT-based SOMs in the TriPleX platform at 2.5 MHz. This demonstration is not part of an early characterization process, but part of a complete system demonstration of a compact LDV system based on photonic integrated OFS units. In the first version of the system, the OFS is based on a cascade of PZT-based SOMs driven by sawtooth function that enables bandwidth demanding serrodyne modulation up to 100 kHz, while in the second version, it is based on a quad array of PZT phase shifters inside an IQM that enables SSB modulation up to 2.5 MHz. In both versions, the TriPleX photonic integrated circuit (PIC) with the OFS unit is combined with an external beam scanning unit for the emission of the sensing beam, the collection of the reflecting light and the execution of the beam scanning process, and with A second PIC developed in the optical polymer platform called PolyBoard [40]. Thanks to the intrinsic possibility of the PolyBoard for polarization handling of the waveguided light and for low-loss hybrid integration of indium-phosphide (InP) components [41–43], this second PIC is used in our compact LDV system for polarization split and rotation of the light in the sensing and the reference arm of the system, and for execution of the heterodyne detection in both polarizations by means of on-chip InP balanced detectors. System evaluation of the compact LDV and benchmarking against gold-standard, bulky LDV equipment confirms the potential for high-quality displacement measurements with resolution below 10 pm for vibration frequencies up to hundreds of kHz.

The remainder of the manuscript is organized as follows: In section Methods, we first describe the operation principle of heterodyne LDVs. We then introduce our modelling for the OFS schemes of the serrodyne frequency shifter (SFS) and the SSB-OFS, and we theoretically investigate their performance in the presence of imperfections that exist in practical implementations. Subsequently, we present the design and fabrication of the TriPleX and PolyBoard PICs, realizing the frequency shift and the coherent detection respectively, and we describe the PZT structures for the stress-optic modulation in TriPleX. In section Heterodyne LDVs, we first present characterization results for the OFS PICs in TriPleX, and next we describe the experimental setup of the miniaturized LDV system and present our results from the vibration measurements. We discuss our results and compare them with the theory presented in section Methods. Finally, in section Optical Frequency Shifter (OFS) modelling, we outline our next steps, and conclude.

Methods

Heterodyne LDVs

In an LDV the velocity information $\upsilon(t)$ of a vibrating surface is transformed to a Doppler frequency shift $f_D(t)$ in the optical signal, that corresponds to an instantaneous phase shift $\varphi_D(t)$, described by

$$f_D(t) = \frac{d\varphi_D(t)}{dt} = \frac{2n}{\lambda}\upsilon(t)\,, \tag{1}$$

where λ is the wavelength of the laser source and n the refractive index. The information in the phase of the optical signal is extracted with the help of an interferometer. The latter is formed by splitting the light from a laser source into two parts: the measurement and the reference signal. The measurement signal is sent to the vibrating surface, where it is reflected and scattered. A small portion of the light is collected and coupled back into the interferometer to be recombined with the reference signal. In a heterodyne LDV, a frequency shift f_0 is introduced to the optical frequency f_{opt} of either the measurement or the reference signal, to introduce directional sensitivity to the measurement. The reference signal is expressed as

$$E_r(t) = E_r exp\left(j2\pi f_{opt}t\right),$$ (2)

and the collected measurement signal can be written as

$$E_m(t) = \sqrt{a}E_m exp\left\{j\left[2\pi\left(f_{opt}+f_0\right)t + \varphi_D(t)\right]\right\},$$ (3)

where a the attenuation factor due to the scattering, reflection, and propagation loss of the signal. The combined signal is sent to a photodetector that produces a photo-current according to the beating signal, given by

$$I \propto |E_m(t) + E_r(t)|^2 = I_r + I_m + I_{het}(t),$$ (4)

where $I_r = (E_r)^2$, $I_m = a(E_m)^2$, and

$$I_{het}(t) = 2\sqrt{a}E_r E_m\cos[2\pi f_0 t + \varphi_D(t)]$$ (5)

The dc terms I_r and I_m are filtered out, while the I_{het} is sent to the demodulator. Demodulation can be performed either in the analog domain, using a frequency-to-voltage converter or in the digital domain, by sampling the signal $I_{het}(t)$ and using digital signal processing (DSP) techniques [44, 45]. Although good performance can be achieved with analog demodulation, digital approaches provide better performance in terms of stability and linearity, with the arctangent phase IQ demodulation being the most popular method for decoding the LDV signal [46].

Optical frequency shifter (OFS) modelling

Two modulation schemes have been reported as suitable for implementing OFS with integrated planar waveguide circuits: the serrodyne and the SSB OFS. In the following paragraphs we present their operation principle, their basic trade-offs and limitations, and we model their performance.

Serrodyne frequency shifter (SFS)

Serrodyne frequency shift is based on the modulation of the phase of an optical carrier E_{in} with a linear phase ramp. The linear increase of the optical phase in the time domain, i.e. $\varphi(t) = 2\pi f_0 t$, shifts the frequency of the output optical signal by f_0:

$$\begin{aligned}E_{out} &= E_{in}e^{j\varphi(t)}\\ &= E_0 e^{j(2\pi f_{opt}t + \varphi(t))},\\ &= E_0 e^{j2\pi(f_{opt}+f_0)t}\end{aligned}$$ (6)

where E_0 is the amplitude and f_{opt} is the frequency of the input signal's electric field. A linearly increasing phase profile can be realized by driving the phase modulator with a sawtooth signal of period $T_0 = 1/f_0$ and with an amplitude such that a total of 2π shift is inserted, as shown in Fig. 1b. In the ideal case, the falling time τ_f of the sawtooth is infinitely small relative to the period T_0, and the optical phase increases in a continuous manner. The input optical power is shifted entirely to the desired frequency $f_{opt} + f_0$. In a practical implementation though, where the ratio τ_f/T_0 cannot be infinitely small due to bandwidth limitations, the phase ramp of the optical field will be disrupted for an amount of time equal to τ_f in every period. Thus, a portion of the input optical power will appear in harmonic sidemodes in the optical spectrum around the frequency shifted carrier and the modulated optical signal is described by

$$E_{out} = E_{in} \sum_k a_k e^{j2\pi(f_{opt}+kf_0)t}, k \in Z, \tag{7}$$

where k is the order of the harmonic sidemode and a_k the corresponding amplitude [47].

Figure 1c shows the simulated output optical spectrum produced with a modulating sawtooth of frequency $f_0 = 0.1$ MHz for the cases of infinitely small and finite falling time. We define the falling time as the interval between the end of the rising slope and the beginning of the next one, from maximum to minimum point, as it is depicted in Fig. 1b. In the case of a perfect sawtooth the sidemode suppression ratio (SMSR), i.e.,
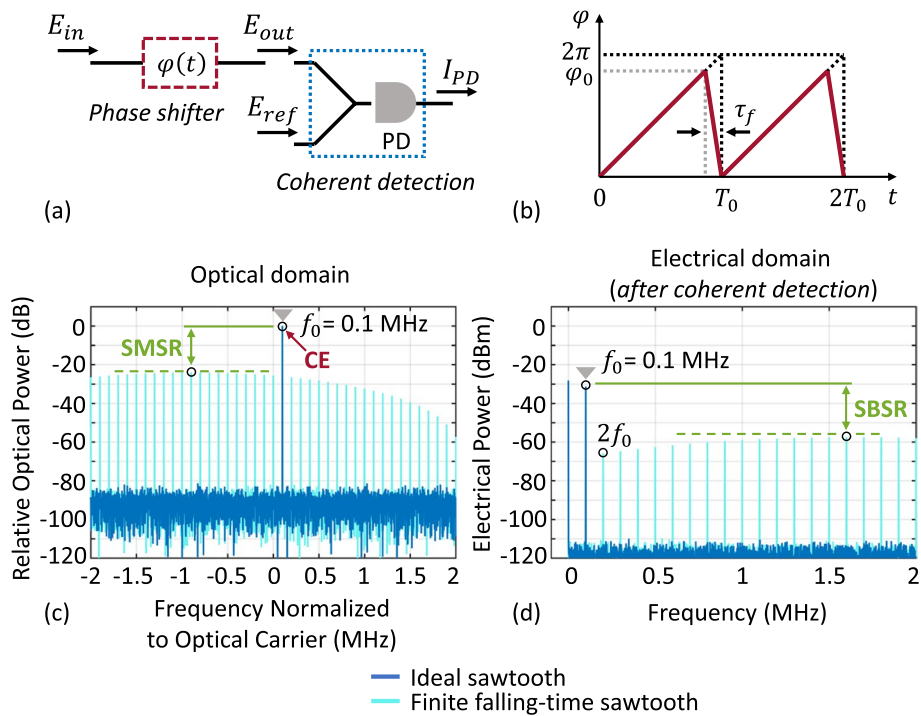

Fig. 1 a Illustration of the simulation setup for the serrodyne OFS and **b** the sawtooth phase modulation with period $T_0 = 1/f_0$. **c** Output optical spectrum for modulation frequency $f_0 = 0.1$ MHz. The blue spectrum corresponds to an ideal sawtooth with infinitely small falling time. The yellow lines appear in the case of sawtooth with finite falling time (0.05 T_0). **d** The electrical spectrum after the coherent detection. The sidebands in the electrical spectrum are created from the down-converted side-modes present in the optical spectrum around the frequency shifted carrier at $f_{opt} + f_0$ s

the ratio between the fundamental frequency and the highest sidemode, is only limited by the noise floor, while in the sub-optimal case the presence of harmonic sidemodes deteriorates the SMSR (Fig. 1c). The amount of the input optical power that is shifted to the desired frequency $f_{opt} + f_0$ is not significantly deteriorated, preserving the high conversion efficiency (CE) of the SFS. Figure 2a shows in more detail the impact of the sawtooth falling-time on the SMSR and the CE performance. A falling-time of less than 1% of the sawtooth period is required to keep the SMSR above 40 dB, while the deterioration of CE is limited to less than 2 dB, even if the falling-time reaches 20% of the period. The high conversion efficiency is one of the main advantages of the serrodyne technique, which makes it a considerable candidate for sensing applications with strict requirements in optical power budget. The limiting factor is the large bandwidth required to accommodate the sawtooth modulation. To achieve good SMSR performance, both the optical modulator, as well as the driving circuit must exhibit analog bandwidth significantly larger than the fundamental frequency of the desired shift f_0 e.g., a 3dB bandwidth of more than 35 f_0 is needed to keep the τ_f/T_0 ratio below 1%, assuming a 1$^{\text{st}}$ order linear system [47].

Since heterodyne LDV systems rely on the coherent detection of the measurement signal using a local reference, it is meaningful to study the impact of an imperfect modulation directly in the electrical domain after the coherent detection. Figure 1d presents the corresponding simulated electrical power spectrum. The modulated optical field E_{out} is combined with an optical reference E_{ref} i.e., a copy of the input field E_{in}, and the beating signal is detected on a photodiode, as depicted in Fig. 1a. As a result of the optical beating, the frequency shifted tone at $f_{opt} + f_0$ is down-converted to f_0 along with the sidemodes, and harmonic sidebands appear in the electrical spectrum after photodetection. To refer to the ratio between the highest sideband and the fundamental at f_0 in the electrical spectrum we use the term sideband suppression ratio (SBSR), to distinguish it from the SMSR used for the optical domain.

Figure 2b shows the impact of the amplitude and falling time of the phase modulation on the SBSR performance. For the first two cases (red and green colored marks), each parameter is sweeping independently from 0 to 20% deviation from the ideal value, while the non-sweeping parameter is kept constant to its ideal value i.e., 2 π for the amplitude
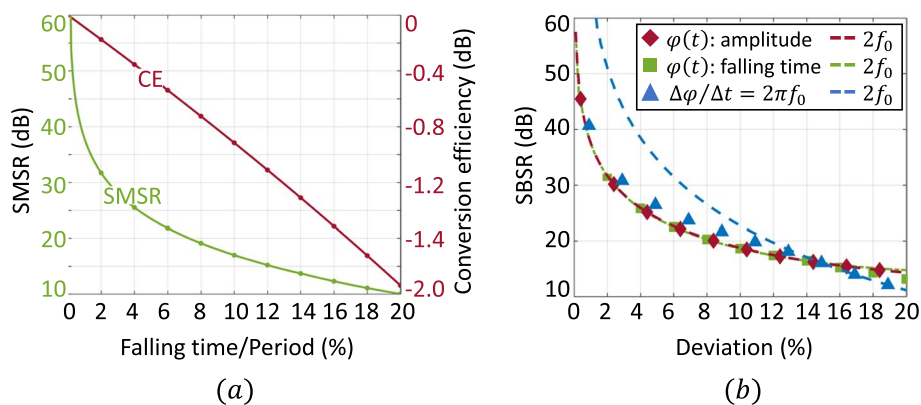
Fig. 2 a Impact of the falling time of the sawtooth waveform on SMSR and CE. **b** Effect of imperfect amplitude and falling time of the modulating sawtooth on SBSR

and 0 for the falling time. In the last case (blue marks), both phase amplitude and falling time are sweeping such that the slope $d\varphi(t)/dt$ is constant and equal to $2\pi/T_0$. The markers indicate the overall SBSR performance i.e., the suppression ratio between the fundamental harmonic and the highest sideband in the output spectrum, where the dotted lines show the suppression ratio between the fundamental and the $2\,f_0$ component. When the amplitude or the falling time are changing independently the dotted lines coincide with the markers, suggesting that the $2\,f_0$ component is the highest sideband which determines the overall SBSR. In the case of constant slope $2\pi/T_0$ the SBSR performance for deviations below 15% is determined from sidebands at positions further away from the fundamental frequency, as the suppression ratio of the $2\,f_0$ component is significantly higher. Since most of the sidebands can be later suppressed through appropriate filtering, it is important to keep the highest sidemodes away from the f_0 component [46]. Moreover, it can be derived that in cases in which achieving a full 2π shift is not possible due to driving limitations, the falling time should be adjusted accordingly such that it holds $\Delta\varphi/\Delta t = 2\pi/T_0$.

SSB frequency shifter

The dual-parallel (DP-) MZM configuration, originally introduced four decades ago, has been used to demonstrate single-sideband (SSB) modulation and frequency shifting [11]. The configuration of the circuit is presented in Fig. 3a. Two MZM are combined in parallel with a relative optical phase shift of π/2 to form an IQ configuration. Each MZM is driven in push–pull mode and is biased at the minimum transmission point, thus an optical phase difference of π is introduced between the two arms. The driving signal is a sinewave of frequency f_0 which is fed into the upper and the lower MZM with a π/2 relative phase shift.

The basic idea behind the frequency shift accomplished with the IQ configuration can be viewed as a two-step process. First, multiple spectral lines are generated in the optical domain through the phase modulation of the input light. The second step is the precise cancelation of the unwanted spectral components through destructive interference. A detailed description of this process is presented in Fig. 3b. The optical input is split into four optical paths and is modulated by four separate phase modulators, each driven by a sinewave of appropriate amplitude and phase. The optical spectrum at the output of each modulator is a set of spectral lines at positions of multiples of the modulation frequency f_0 and with magnitude and phase described by Bessel functions [17]. When the light is combined at the output of each MZM only the odd-order lines survive as the even-order lines have opposite phases and undergo destructive interference. By combining the outputs of the two MZM with a π/2 relative phase shift more lines are excluded from the spectrum, leaving at the output of the SSB-OFS the spectral components at …, $f_{opt} - 3f_0$, $f_{opt} + 1f_0$, $f_{opt} + 5f_0$ etc., described by the expression

$$E_{out} = E_{in} \sum\nolimits_{k=4n+1} J_k(a) exp\left[j2\pi\left(f_{opt} + kf_0\right)t\right], n \in Z, \tag{8}$$

where $J_k(a)$ is the k-th order Bessel function of the first kind, a the amplitude of the phase modulation with frequency f_0, assuming uniform excitation, and f_{opt} the frequency of the input optical signal. From Eq. (8) becomes apparent that even in the ideal case where all the spurious side-modes that undergo destructive interference throughout
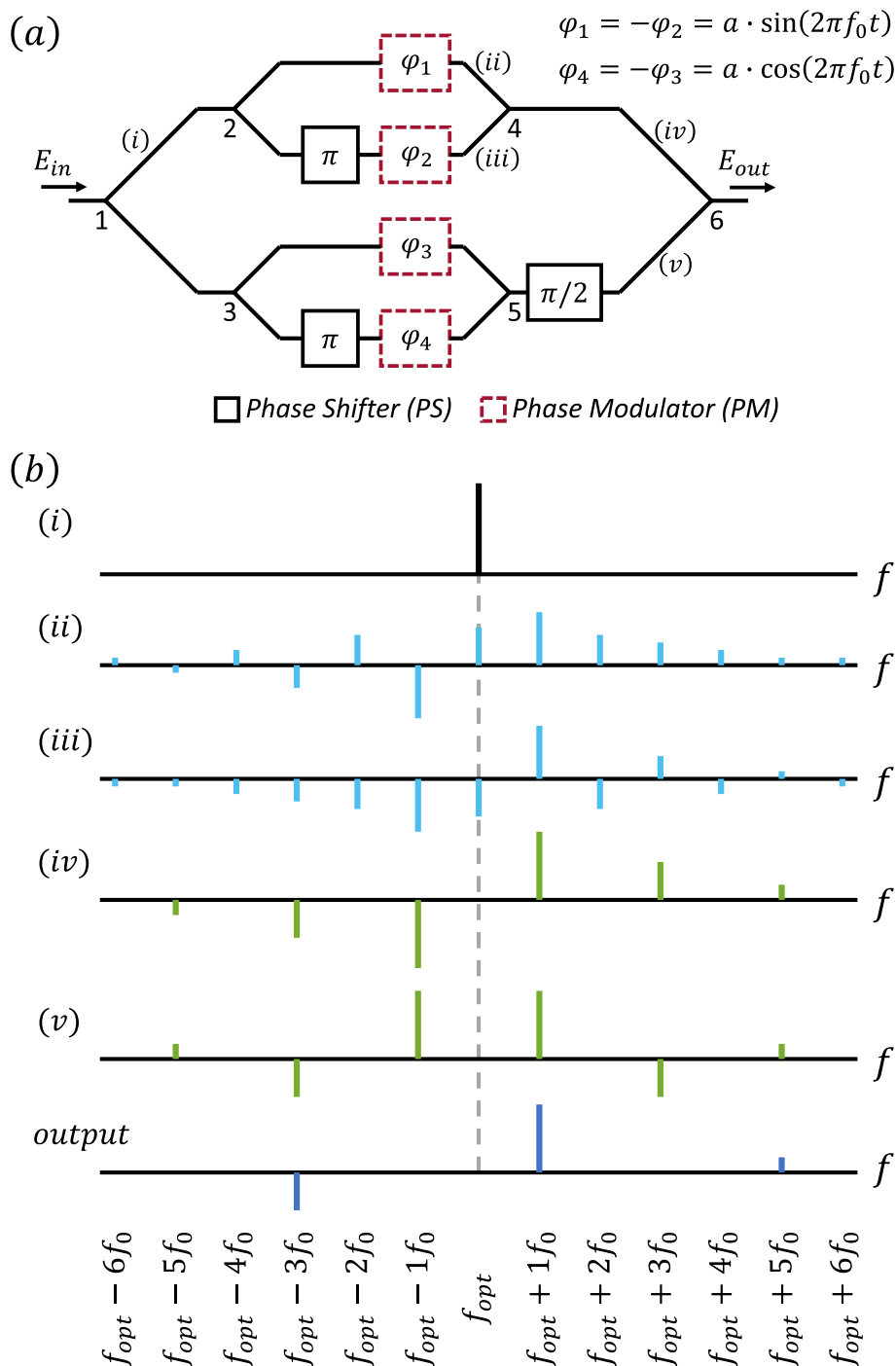
Fig. 3 a Schematic of the SSB-OFS and **b** the field amplitude spectrum at different points of the circuit

the circuit have been completely removed, unwanted side-modes are still present in the output spectrum around the fundamental component $f_{opt} + f_0$ of the desired frequency shift. If the $\pi/2$ phase shift is assigned to the other arm of the circuit the optical spectrum is flipped around f_0, and the fundamental frequency becomes $f_{opt} - f_0$. Both the up-shifted and down-shifted carriers can be generated simultaneously by utilizing the

complementary outputs of a 3dB directional coupler for the combination of the I and Q arms [13, 15].

Stronger modulation generates higher side-modes in the optical spectrum due to the non-linear transfer function of the MZM. Thus, high SMSR performance requires driving in small-signal regime, in the expense of low CE. This characteristic trade-off of the IQ topology is presented in Fig. 4d. The maximum CE, equal to -4.7dB, is present for a phase modulation peak-to-peak amplitude of 1.176π, where the SMSR is limited to 14.8 dB, under the assumption of optimal configuration. For the rest of our analysis, we assume a peak-to-peak amplitude of 0.2π, which corresponds to a CE of -16.2 dB and
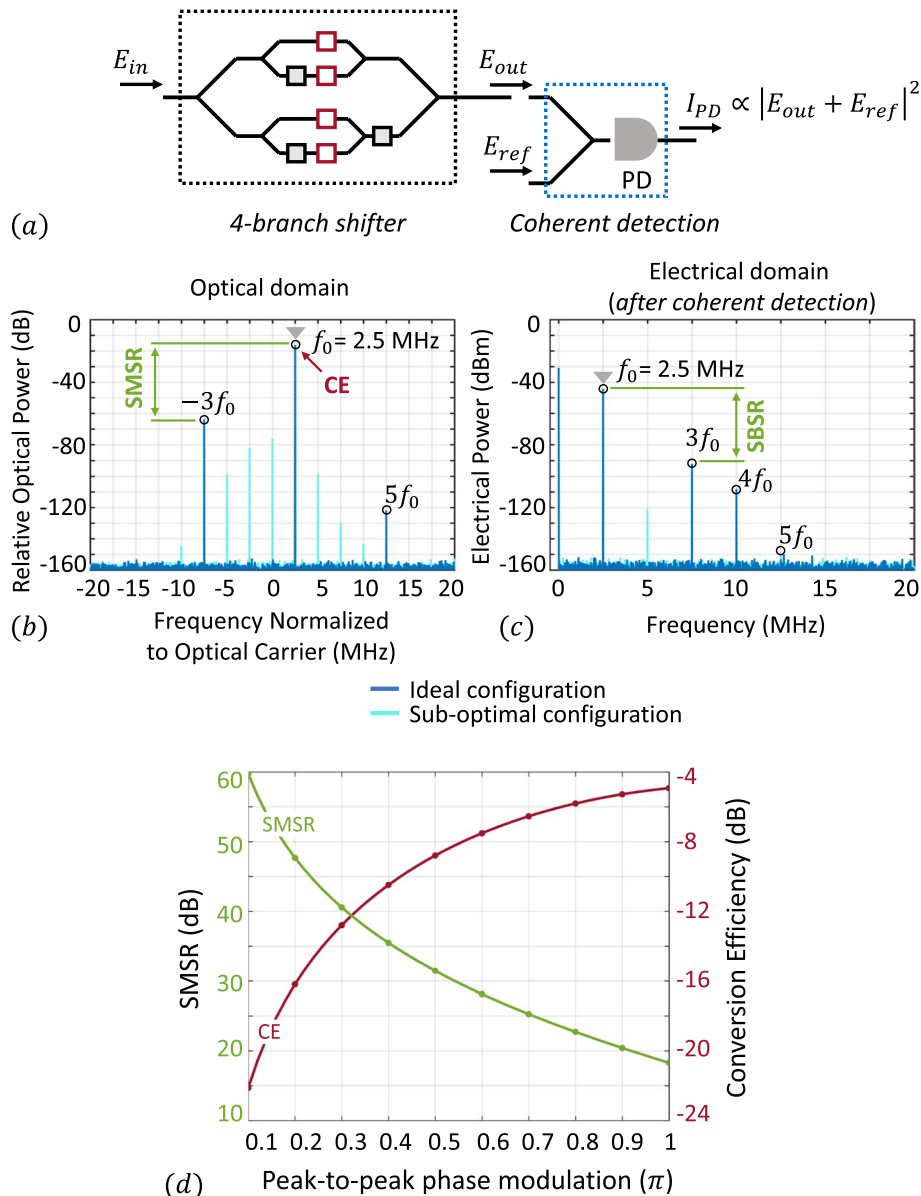
Fig. 4 a Block-diagram of the simulation of the coherent detection. Simulated spectrum in the **b** optical domain and in the **c** electrical domain after coherent detection of the output of the SSB-OFS. **d** CE and SMSR determined/imposed by the driving amplitude

an SMSR of 47.7 dB in ideal configuration. An approach to overcome the limitations posed by this trade-off has been demonstrated by utilizing pre-distorted driving signals to compensate for the non-linear transfer function of the MZM [17].

Figure 4b presents the simulated optical output of the SSB-OFS shifter for the case of optimal and a random sub-optimal configuration of the device, with the modulation frequency f_0 at 2.5 MHz. For the sub-optimal case, spectral lines are present in multiples of the modulation frequency. After the coherent detection, the spurious side-modes of the optical domain are down-converted and appear as sidebands in the electrical spectrum, as presented in Fig. 4c, deteriorating the SBSR. In the ideal case of a perfect circuit, in which only the terms of Eq. (8) are present, SMSR and SBSR are equal, as they are both determined by the height of the 3 f_0 component. In a sub-optimal configuration though, the beating of the reference carrier signal with the output of the SSB-OFS generates a spectral line at 2 f_0, which can become larger than the 3 f_0 component and further limit the SBSR.

Three main factors are responsible for maintaining the desired symmetry between the cancelling spectral components. First is the phase modulation depth. Exactly equal phase modulation should be inserted into each of the four modulation branches. This translates to the need for calibration of the driving amplitudes in the case of non-uniform modulation efficiency between the modulators. The suppression of the spectral lines that undergo destructive interference relies on the precision of the power splitting ratio of the splitting and combining components (extinction ratio relationship), which can be realized as Y-branches, directional couplers or tunable MZIs. The third factor is the dc optical phase shift that is needed for the biasing of the two MZM at the zero-transmission point, as well as for the π/2 phase shift between the MZM. Another factor is the relative phase shift between the driving signals, but since in most of the cases a common oscillator is used for their generation, the same phase noise is shared among the signals, thus the impact on the SBSR is negligible.

We investigate the impact of the above factors on the performance of the SSB-OFS. To evaluate the performance, we use the spectrum of the electrical signal, that is produced on the photodiode from the beating of the frequency shifted signal with the optical carrier, as depicted in Fig. 4a. The phase modulation depth is set to 0.2 π peak-to-peak for the analysis. We introduce a deviation from the ideal value of each parameter (up to 20%) and calculate the SBSR in the spectrum. We assume that all the other parameters of the circuit, except for the sweeping one, take their ideal values. Figure 5a shows the impact of unbalanced phase modulation among the four branches. The dotted lines represent the suppression ratio of the component at 2 f_0, while the solid line shows the total SBSR performance. The deviation of the phase modulation depth from the set value (0.2π) is swept from 0 to 20%, for each one of the four modulators. For small deviations the configuration is close to the ideal, and the SBSR is limited by the spectral line at 3 f_0. In this case the SBSR is equal to 47.7 dB (see Fig. 4c-d). For large deviations, the spectral line at 2 f_0 exceeds the one at 3 f_0, and the SBSR is determined by the 2 f_0 components. Each of the four modulators has a different impact on the overall SBSR. A small deviation of only 4% in the phase modulation φ_4 will deteriorate the overall SBSR, while a deviation of more than 15% is needed for φ_3 to cause the same effect. This asymmetry is related to the way in which the different spectral lines, that are produced from the phase modulation,
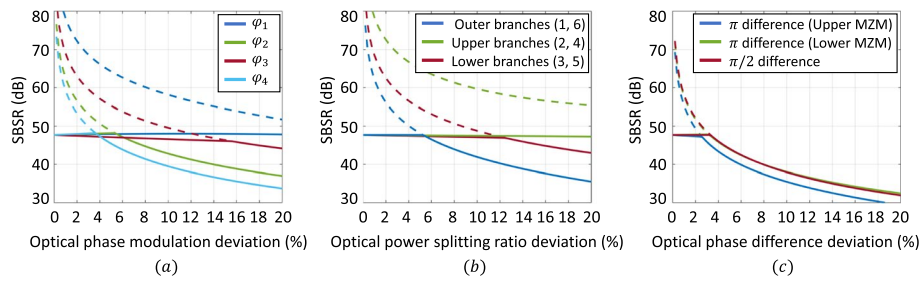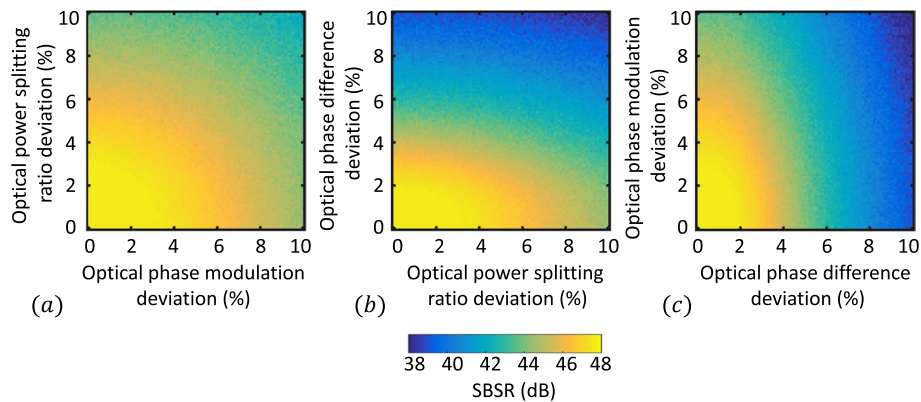
Fig. 5 Simulated suppression ratio of the sidebands at the output of the SSB-OFS with relation to the deviation of **a** the phase modulation, **b** the power splitting ratio and **c** the phase difference of the optical circuit. The suppression ratio of the sidebands is measured in the electrical domain (SBSR) after coherent photodetection. Phase modulation of 0.2 π peak-to-peak is assumed

are combined through the optical circuit. A detailed description can be derived using the Bessel functions [17], but such an in-depth analysis is beyond the scope of this work. In Fig. 5b the SBSR performance is presented with respect to the deviation from the ideal 50:50 optical power splitting ratio of the splitting and combining elements of the circuit. The symmetrical power splitting in the outer MZI, formed by branches 1 and 6 (see Fig. 3a), is the most critical, as a deviation above 5% from the exact 50:50 ratio can deteriorate the SBSR. A deviation of more than 12% at the branches of the lower MZM will deteriorate the SBSR, while the deviation of the branches of the upper MZM has no impact on the SBSR even for values up to 20%. The unequal effect of the upper and the lower MZM on the SBSR is again related to the way that the spectral lines interfere throughout the circuit. The accurate configuration of the phase difference between the optical paths of the MZMs is also critical. As it is shown in Fig. 5c, inaccuracy from the exact value of less than 4% will start to deteriorate the SBSR.

The analysis presented in Fig. 5 assumes that except from the sweeping parameter, the rest of the circuit is ideal. Each parameter acts independently on the performance, while all the other parameters take their ideal values. Although this kind of modelling demonstrates the significance of each parameter, it fails to capture the performance of the SSB-OFS in a real scenario, in which all the factors act in combination. To provide this insight, we run Monte-Carlo simulations in which the phase modulation, the optical power splitting ratio and the optical phase difference are considered in pairs, with their deviation taking random values from the interval [0, 0.1] with a uniform distribution for 200 trials. The results of the simulation are presented in Fig. 6. With respect to SBSR it can be derived that the most critical parameter is the optical phase difference between the paths of the MZIs, while a less than 1.2 dB degradation of the CE was observed.

Design and fabrication

Two different types of PICs were developed for the heterodyne LDV system: the first in TriPleX, comprising the stress-optic PZT modulators for the optical frequency shift (OFS) and the second in PolyBoard, realizing the receiving part of the system. In TriPleX both an SFS and an SSB-OFS were designed and fabricated.

Fig. 6 Simulated side band suppression ratio (SBSR) at the output of the SSB-OFS after coherent detection. The effect of the deviation of **a** the phase modulation, **b** the power splitting ratio and **c** the phase difference between optical paths of the optical circuit from their ideal values is demonstrated in pairs

TriPleX circuit and stress-optic modulation

TriPleX is a photonic integration platform based on Si_3N_4 (silicon nitride) and SiO_2 (silicon dioxide), offering single mode operation, low propagation losses (0.1 dB/cm at 1.55 μm) and high integration density over a wide wavelength range (0.4 μm – 2.35 μm) [48]. The high contrast between the refractive index of the silicon nitride core material (~1.98) with respect to the silicon oxide cladding material (1.45) supports the realization of waveguiding structures with strong confinement profile that enable the actualization of compact photonic circuits. A wide variety of waveguide geometries that support the propagation of TE polarized light is provided, such as box, single stripe, symmetric or asymmetric double stripe. Based on these geometries, a palette of standardized building blocks is provided that are manufactured in a single monolithic process flow with CMOS-compatible tools.

In our designs, the asymmetric double stripe (ADS) geometry was used, optimized for low-loss propagation of the fundamental TE-mode at 1.55 μm. This consists of two Si_3N_4 stripes with unequal heights (core material) in a top–bottom configuration, surrounded by SiO_2 (cladding material). The height of the bottom and the top Si_3N_4 stripe is 75 and 175 nm respectively, with 100 nm SiO_2 layer in between. Wet thermal oxidation is used to create the bottom cladding SiO_2 layer on top of a single-crystal silicon substrate, typically at temperatures equal to or above 1000 ℃. Low pressure chemical vapor deposition (LPCVD) is used for the Si_3N_4 layers. The SiO_2 top cladding layer is formed with the combination of TEOS (using the gas tetraethylorthosilicate) LPCVD deposition and plasma-enhanced chemical vapor deposition (PECVD), to create cladding thicknesses of at least 8 μm. Typical deposition temperatures are between 300 ℃ and 400 ℃. The waveguide structures are specified with E-beam lithography (EBL), while deep reactive ion etching (DRIE) is used to embed the pattern after resistive development.

An attractive feature of the TriPleX toolbox is the possibility to realize phase tuning elements based on the stress-optic effect, by depositing a thin layer of piezoelectric material on top of the waveguiding structures. The piezoelectric material of lead zirconate titanate (PZT) is used, due to its relatively large effective piezoelectric coefficients ($d_{33f} > 200$ pm/V and $e_{31f} > 18$ C/m^2) [38]. In the conventional approach, the PZT layer is

deposited between a top and a bottom Platinum (Pt) electrode, forming a top–bottom configuration. By applying a voltage between the two electrodes, the PZT layer expands and contracts due to the piezoelectric effect, causing stress to the waveguiding structure underneath. This stress results in phase modulation of the propagating TE-mode, due to the change of the refractive indices of the SiO_2 and Si_3N_4 layers, and, consequently, of the effective refractive index of the mode. With this configuration, stress-based phase shifters can support tuning frequencies at least one order of magnitude higher than conventional phase heaters (PHs) in TriPleX, while they offer significant reduction in the steady state power consumption (by a factor of 10^6) relative to their thermo-optic counterparts [29–32]. As an electrical load, the PZT-based SOM is characterized by the typical crystal model, which exhibits capacitive behavior when the excitation frequency is not close to its resonance. The capacitance is primarily formed by the upper and bottom electrodes that are separated by the non-conductive PZT layer. While ultra-low power consumption can be achieved in steady state operation due to the capacitive nature of the structure, the power increases linearly with the modulation frequency f, limiting the bandwidth of the device. The power dissipation is proportional to the capacitance C, the modulation frequency f and the square of the applied voltage V,

$$P = CV^2f \tag{9}$$

In this work, an alternative structure was developed to increase the bandwidth of the device by lowering the capacitance between the two electrodes, to make it more suitable for modulation. In the top–bottom configuration the distance of the electrodes is defined by the thickness of the PZT layer, which is fixed to 2 μm for optimum stress-optic modulation of the effective refractive index. By placing both electrodes on top of the PZT layer, their position can be selected freely and thus optimized. With the top-top configuration shown in Fig. 7, a capacitance of 100 pF is achieved, an order of magnitude lower from what is possible with the top–bottom configuration. When growing the PZT layer on top of SiO_2, usually an intermediate seeding layer is used to enhance the growth of the piezoelectric layer. In the case of the conventional top–bottom electrode configuration the seeding layer material that is widely used is LNO (Lanthanum Nickel Oxide). However, the conducting nature of the latter makes it unsuitable for the top-top
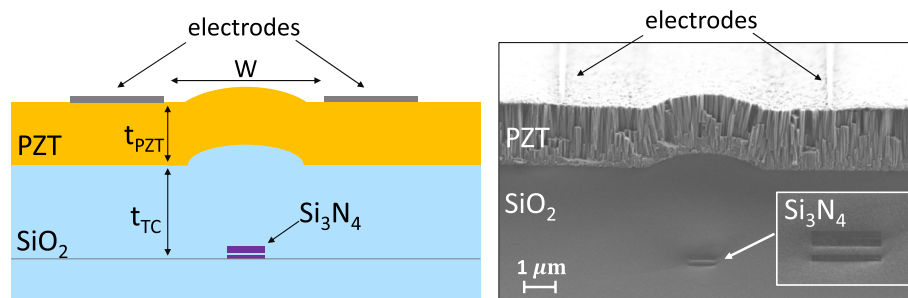

Fig. 7 Illustration of the PZT thin film on top of the TriPleX structure (Left) and a corresponding SEM picture (Right). Both electrodes are placed on top of the PZT layer (top-top configuration) with a gap (W) of 9 μm. The thickness of the PZT layer (t_{PZT}) is 2 μm. The ADS waveguide is buried under 3 μm of SiO2 top cladding (t_{TC})

configuration, as a non-conducting layer is required below the PZT structure. The proposed non-conducting material for the seeding layer is BTO (Barium Titanate), which demonstrates good material growth directly on SiO_2. A Pulsed Laser Deposition (PLD) growth method built by Solmates is used to deposit the BTO/PZT bilayer on a wafer-level [39, 49, 50]. To increase the efficiency of the modulator, a dome structure is used to focus the stress on the waveguide [30–32]. The length of the final stress-optic modulator structure is 15 mm.

The TriPleX PIC of the SSB-OFS is presented in Fig. 8. The serrodyne OFS PIC is a simplified version of the same circuit, that does not include the MZIs sections. The dimensions of both PICs in TriPleX are 11.25 mm × 6.9 mm. Figure 9 presents the schematic layout of the OFS circuits. The serrodyne frequency shifter (Fig. 9a) comprises a
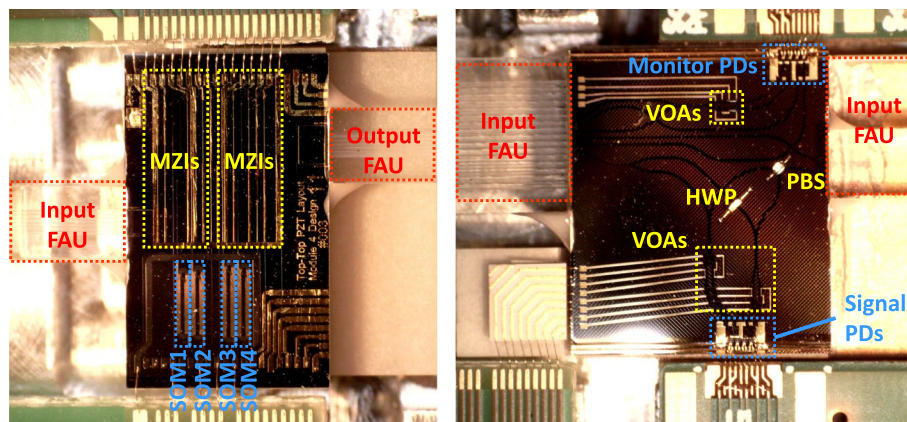
Fig. 8 (Left) Top view photograph of the TriPleX PIC with the SSB-OFS. The circuit comprises 7 MZIs controlled by phase heaters and 4 PZT-based stress-optic modulators (SOMs). (Right) Top view photograph of the PolyBoard PIC implementing the dual-pol coherent receiver. The micro-optic elements of the polarization beam splitter (PBS) and the half-wave plate (HWP) are visible on the chip
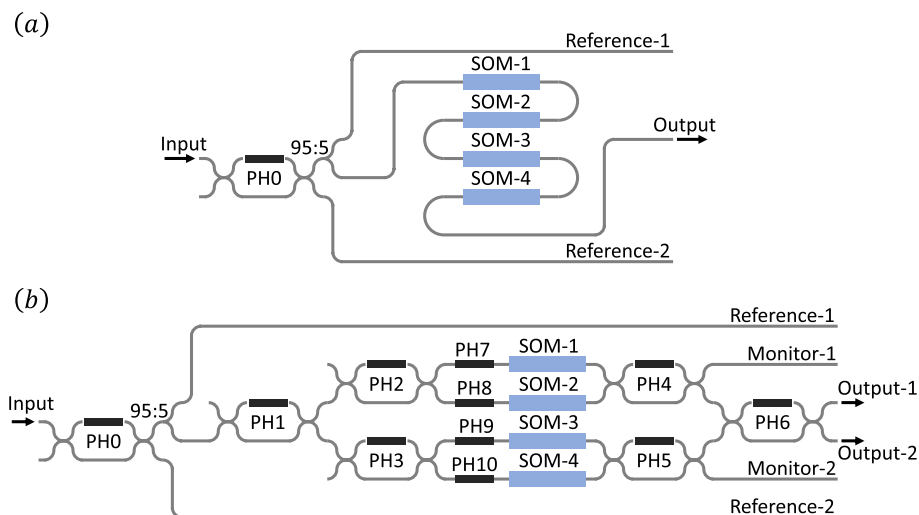

Fig. 9 Schematic of the circuit of **a** the serrodyne and **b** the SSB optical frequency shifter (OFS) in TriPleX. Phase heaters (PH) are used for the control of the MZIs and stress-optic modulators (SOMs) for the optical modulation

tunable MZI at the input, based on thermo-optic tuning, which is responsible for splitting the inserted light into the measurement and the reference path. A small portion of the light in the measurement path is split with a 95:5 coupler and is outcoupled from a monitor port. The largest portion of the light in the measurement path is guided towards the OFS section, where it is modulated by the stress-optic PZT modulators. Four stress-optic modulators are integrated in series to distribute the total 2π phase among multiple elements and lower the required driving amplitude. A much more complex circuitry constitutes the SSB-OFS (Fig. 9b), that comprises 7 tunable MZIs and a total of 10 phase heaters (PHs). To test this device, careful characterization of all tunable elements must be performed. Input light is split to the measurement and the reference path with the help of an MZI, and the reference part is outcoupled from the PIC. For monitor purposes a portion of the light in the measurement path is also outcoupled from the chip using a 95:5 coupler, similar to the circuit of the serrodyne shifter. The optical frequency section consists of two push–pull MZMs. Precise control of the splitting-combining ratio of the MZMs is offered by the tunable MZIs, allowing the configuration of the device to achieve optimum performance.

Receiver circuit in PolyBoard

The second photonic platform, that is used for the implementation of the detection part of the integrated LDV, is PolyBoard. PolyBoard is a polymer-based multifunction photonic platform, offering a single-mode operation, low propagation losses (0.7 dB/cm at 1.55 μm), and the possibility for integration of polarization handling elements [40] and indium-phosphide (InP) components [41–43, 51]. The core and the cladding have refractive indexes of $n_{core} = 1.48$ and $n_{clad} = 1.45$ respectively, supporting both the transverse electric (TE) and magnetic (TM) components, because of the waveguide symmetry which is rectangular with thickness in both axes of 3.2 μm. The single-waveguide PolyBoard stack consists of a waveguide and a cladding resin and is realized by using procedures of consecutive layer deposition. The fabrication of the PolyBoard chip, comprises the spin-coating of the cladding resin on the silicon (Si) substrate, the spin-coating of the waveguide resin, the structuring of the waveguiding layer with reactive ion etching (RIE) and ultraviolet (UV) lithography, and the spin-coating of the second layer of cladding resin to create the top cladding layer.

Figure 8 presents the PolyBoard PIC and Fig. 10 the schematic of the corresponding circuit. On the west side the TE polarized-reference signal is coming from the laser source. Then, it is divided into two parts after passing through a 50:50 coupler. One of the two TE components is rotated by 90 degrees by using a half-wave plate (HWP), creating two reference beams (TE and TM) as local oscillators (LOs) for heterodyne detection. The measurement light is coupled into the PIC from the east side with arbitrary polarization. To handle the polarization state of the measurement light and split it into a TE and a TM component, an integrated polarization beam splitter (PBS) is used [51]. The two components are mixed with the corresponding LO in one 2×2 multimode interference (MMI) coupler respectively. The balancing of the optical power between the reference and the measurement signals prior to the mixing is achieved by the combination
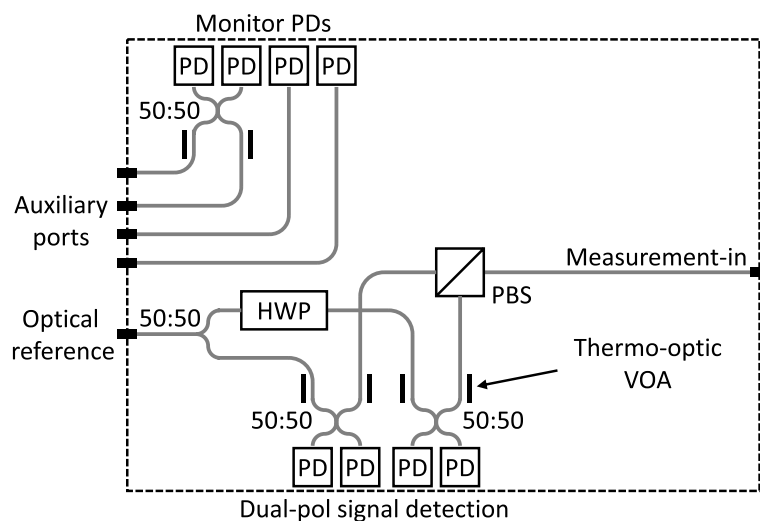
Fig. 10 Schematic of the dual-pol coherent detection circuit in PolyBoard

of the 2×2 MMIs with thermo-optic-based variable optical attenuators (VOAs) [52]. Finally, the TE and TM mixed signals are guided to four InP-based photodiodes (PDs), realizing a dual-pol coherent detection scheme. Additional photodiodes are placed on the top side of the circuit for monitor and testing purposes. The size of the PolyBoard PIC is 11.25 mm $\times$ 9.6 mm.

Results and discussion

In this section we present the main results that were obtained from the experimental testing of the fabricated devices. We first present the characterization of the OFS PICs and compare with the results of the modelling from section Methods. We then present our results from vibration measurements using a complete LDV system based on a test probe-head from Polytec and its software for signal processing and demodulation [53].

OFS characterization

To evaluate the performance of the optical frequency shifting realized with the fabricated devices we used the setup depicted in Fig. 11. A continuous wave (CW) laser source provides TE light at 1550.12 nm wavelength with ultra-low linewidth, below 2 kHz. After passing through an optical isolator to prevent undesired back-reflections, the light is split into two paths: the modulation and the reference path. Optical power of 6.3dBm in the modulation path is coupled into the PIC with the appropriate TE polarization that is required for efficient coupling to the TriPleX. The output of the PIC is combined with the reference path via a fused fiber coupler and the optical beating is observed on a photodiode. The power spectrum resulting from the photodiode's current in a 50 Ohm resistance is captured with the spectrum analyzer. Dedicated electronics were used for the control of the low-speed thermo-optic phase shifters and for driving the SOMs in the MHz regime. A commercial high-voltage amplifier was also used for driving the SOMs with a sawtooth signal up to 100 Vp-p at 100 kHz frequency.
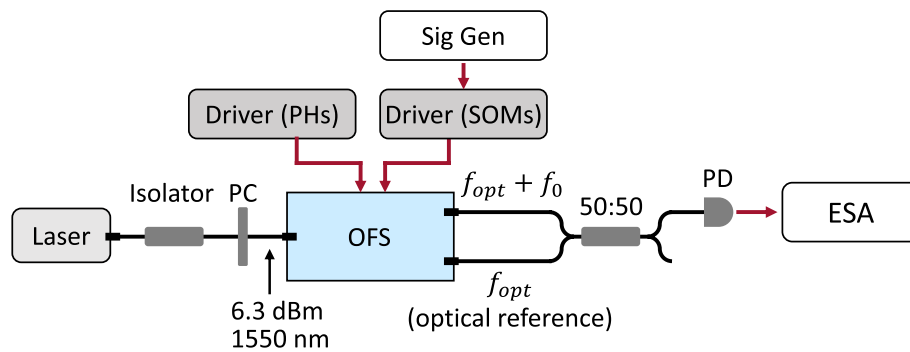
Fig. 11 The setup that was used for the characterization of the OFS PICs. PC: Polarization controller, PHs: Phase heaters, ESA: Electrical spectrum Analyzer

Figure 12 presents the experimental results from the characterization of the stress-optic serrodyne frequency shifter. The spectrum of the acquired beating signal is shown in Fig. 12a. Figure 12b shows the sawtooth driving signal in the time domain, along with the beating signal from the photodiode. The modulation frequency is 100 kHz. The SBSR is 22.1 dB, limited by the 2 f_0 spectral component. As we discussed in the simulation and modelling section, a significant factor for the SBSR performance is the quality of the sawtooth phase profile, in terms of bandwidth and amplitude. From the signals in the time-domain (Fig. 12b) we can see that the discontinuity in the phase modulation due to the sawtooth falling time is approximately 6% of the total period. The manifestation of this discontinuity in the beating signal is practically an inverse modulation caused by the falling slope of the sawtooth. The result is the same sinusoidal waveform as the one produced from the rising slope of the sawtooth, but significantly faster. Two SOMs were driven in series to reduce the required driving voltage for achieving a full 2π shift. A 90% of 2π was accomplished with 100 V peak-to-peak driving amplitude. According to the simulation results presented in Fig. 2b, the quality of the experimentally realized sawtooth is expected to limit the SBSR at 23.8 dB. The 1.7 dB difference between the theoretical and the experimentally measured SBSR may arise from small non-linearities in the response of the stress-optic PZT modulators that become apparent when the amplitude of the driving signal exceeds their polling voltage [32]. The measured CE was approximately -1 dB, assuming total optical losses (coupling and propagation loss) of 5.2 dB.
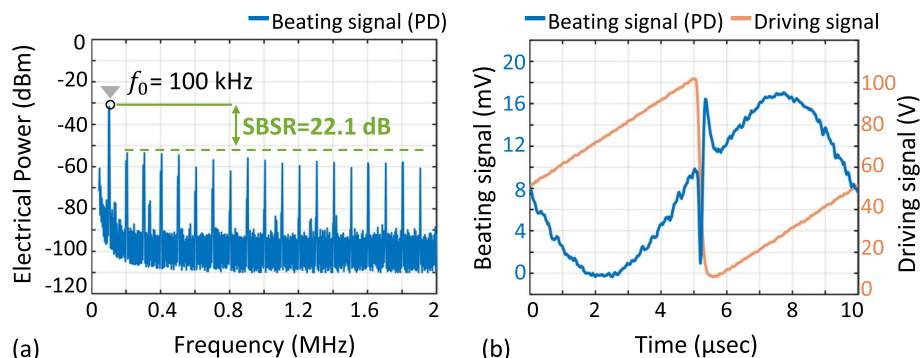

Fig. 12 Experimental results for the serrodyne frequency shifter at 100 kHz

Higher modulation frequencies are possible with the IQ topology of the SSB-OFS since the sinewave driving signals that are used are much less bandwidth-demanding for the driving electronics. Figure 13a presents the power spectrum obtained for a frequency shift at 2.5 MHz. The 2 f_0 component at 5 MHz imposes a 39 dB SBSR, while the suppression ratio of the 3 f_0 is equal to 43.8 dB. The phase shift inserted by the stress-optic phase modulators was configured to be equal to 0.25π peak-to-peak, which corresponds to a suppression ratio of exactly 43.8 dB for the 3 f_0 sideband, according to the modelling presented in section Methods (Fig. 4). With an input optical power of 7 dBm, the optical power of the frequency shifted component at $f_{opt} + f_0$ was measured -14.0 dBm. Optical coupling and propagation losses of 6.3 dB were determined, suggesting a CE of -14.7 dB, only 0.4 dB less than the prediction of the modelling (Fig. 4).

Unequal driving amplitudes were applied to each SOM, since they exhibited different voltage-to-phase-shift relationship, as shown in Fig. 13b. Amplitudes from 25 Vp-p up to 70 Vp-p were applied to achieve the desired 0.25 π phase shift. The difference in the performance originates from variations in the piezoelectric coefficient among the different structures, which are known to depend on the structural properties of the deposited PZT films [32, 54]. Since the driving amplitudes differ, the power dissipation is also different for each modulator and can be derived with the help of Eq. (9). At the operation frequency of 2.5 MHz, the average power consumption was equal to 660 mW, while the best performing structure (SOM-2) dissipated 156 mW. The fabrication process for the specific PZT structures with the top-top electrode configuration was developed for the first time within the present work, and thus, lacks the maturity of the conventional PZT technology based on the top–bottom electrode configuration, which demonstrates higher homogeneity across the wafer [38].

To characterize the phase-shift efficiency of each SOM we used the on-chip MZIs to translate the inserted phase-shift to intensity modulation. For example, to characterize the SOM-1 we used the MZI controlled by PH2 to split the light between the upper and the lower path, where the SOM-1 and SOM-2 are located, respectively (see Fig. 9). The SOM-1 was driven with a 0–100 Vp-p voltage ramp of 10 μs duration, while no signal was applied to SOM-2. The MZI controlled by PH4 was used to combine the modulated
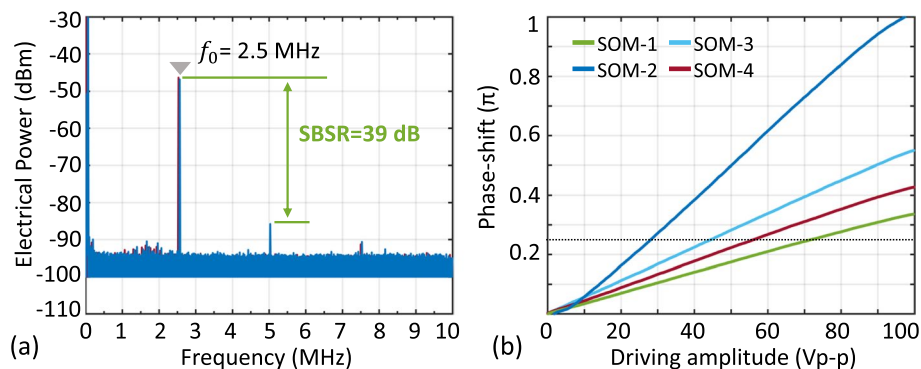

Fig. 13 Experimental results from the testing of the SSB-OFS frequency shifter. **a** Electrical spectrum of the beating signal on the PD. The fundamental frequency shift at 2.5 MHz is visible. The SBSR is 39 dB, limited the 2nd order harmonic sideband at 5 MHz. **b** Phase-shift relative to the applied driving voltage for the four SOMs. The stress-optic response is linear in the interval 10–90 V. The characterization was performed with a rising slope of 100 V peak-to-peak amplitude and 10 μs duration

with the unmodulated light and the optical beating was observed on a PD directly connected to the monitor port-1. The same procedure was followed for the characterization of all the SOMs of the SSB-OFS, accordingly, and the results are presented in Fig. 13b. Before performing any modulation with the SOMs, the device was carefully characterized to identify the correct biasing voltages for the integrated PHs of the circuit and to introduce the appropriate phase-shifts and splitting ratios with the tunable MZIs. Nevertheless, imperfections in the configuration of the device were still present as it is indicated from the fact that the $2f_0$ component is higher than any other sideband. According to the Monte-Carlo simulation results that we presented in section Methods (see Fig. 6), there are deviations within 10% in the inserted phase shift by the SOMs, the splitting ratio of the MZIs and the optical phase shift bias.

The maximum modulation frequency that can be achieved with the PZT-based SOMs is primarily limited by the power bandwidth of the electronics that drive them, since the stress-optic effect can support modulation frequencies in the order of hundreds of MHz [36]. Custom electronics were designed for the driving of the SOMs at MHz range, due to a general lack of readily available commercial options. The need for a sawtooth driving waveform creates high slew-rate and power bandwidth requirements. Additionally, the capacitive nature of the PZT elements presents a high driving current demand, especially during the falling edge of the sawtooth. Existing off-the-self ICs in general can meet these requirements for a tentative 36 Vp-p output swing. Achieving sufficient optical phase-shift with the SOMs called for even higher voltage levels. To this end, we paired a commercial IC with an output voltage transformer (OT), to double the output voltage swing. Utilizing a suitable high-bandwidth, high-power transformer we were able to record a 70 Vp-p amplitude at a 100 pF load from 1 up to 20 MHz.

LDV system

A complete system was realized with the fabricated PICs, as shown in Fig. 14. A low-linewidth fiber-coupled laser provided 10.8 dBm (12 mW) of optical power at 1550.12 nm, which was split into two branches. In the first branch TE polarized light
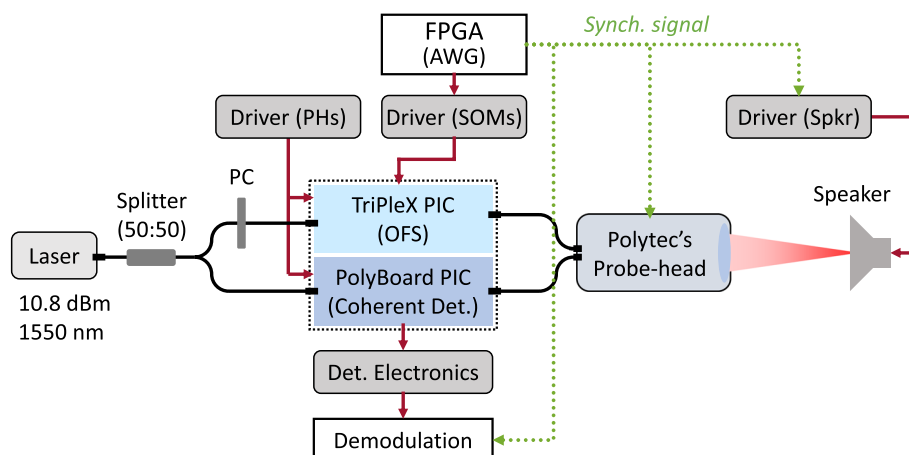

Fig. 14 Setup for vibration measurements. A probe-head from Polytec was utilized for focusing and collecting the light from the vibrating surface. For real-time demodulation a synchronization signal was shared between the driver of the speaker and the demodulation circuit. PC: Polarization controller, PHs: Phase heaters, AWG: Arbitrary waveform generator

with ~ 7 dBm (5 mW) optical power was coupled into the TriPleX PIC that accommodated the optical frequency shift. A frequency shift of 2.5 MHz was introduced by employing the SSB-OFS. The second branch served as the reference beam for the coherent detection in the PolyBoard PIC. Input and output coupling to the PICs was facilitated with fiber-array units (FAU). The frequency shifted output from the TriPleX PIC, serving as the measurement beam, was coupled via fiber into Polytec's probe-head, responsible for focusing the beam on to the vibrating surface under inspection and collecting the reflected light via the same lens system. The measured available optical power for the probe beam was -14 dBm (40 µW). The theoretically inherent loss of the frequency conversion process is 14.7 dB for 0.25π peak-to-peak phase shift, while 6.3 dB corresponds to optical coupling and propagation losses. Custom electronics were used to control the phase-heating electrodes on both PICs, while a separate driving circuit was developed for providing the driving signals to the stress-optic modulators in TriPleX. A dedicated circuit was developed on a field programmable gate array (FPGA) platform to generate the sinusoidal modulation signals with the required phase difference. Another circuit in the FPGA was responsible for providing the necessary clock signals for the synchronization of the driving and detection electronics with the excitation signal of the vibrating surface. The light collected back from the probe-head was coupled into the PolyBoard receiver PIC, where the optical phase information from both TE and TM polarization was detected. The total optical loss in the PolyBoard PIC, including coupling and insertion loss for all optical components in the paths from the fiber-input to the PDs, was estimated at approximately 11 dB for the measurement input, at 15 dB for the optical reference input and at around 15 dB on average for the monitor PDs, assuming PD responsivity of 1 A/W [41]. An additional 9 dB loss was measured in the path of the HWP. The extinction ratio of the PBS was 15 dB. Detection electronics and demodulation software from Polytec were used for the processing of the raw signals.

To test the functionality of the whole setup in terms of accuracy and stability, we performed measurements on a vibration calibrator. The calibrator provided a sinusoidal vibration frequency of 159.15 Hz with a peak-to-peak displacement amplitude of 14.142 µm (10 µm RMS). A stable sinusoidal signal with a displacement amplitude of 14.1 µm was obtained after performing digital demodulation of the raw signal Fig. 15. (Top) presents the displacement spectrum obtained from the FFT of the time trace. A distinct peak from the periodic motion of the calibrator at 159 Hz is visible. The elevated noise up to ~ 35 kHz is probably a result from intermodulation with a spurious frequency component at the electrical carrier frequency of 2.5 MHz. Both the amplitude and the frequency of the demodulated signal matched the expected values of the calibrator, confirming that accurate measurements can be performed with our setup. Considerably lower vibrational amplitudes are needed to test the resolution of the system. For this reason, we performed measurements on a membrane loudspeaker, where displacements in the nm range can be observed. A sinusoidal signal was used to excite the loudspeaker at 15 kHz. The demodulated signal was filtered with a 1 MHz bandpass filter around the 2.5 MHz carrier to reduce the in-band noise and improve the resolution of the measurement. The displacement spectrum is presented in Fig. 15 (Bottom). The 15 kHz excitation frequency of the loudspeaker is clearly visible, corresponding to a displacement of around 5 nm. From the spectrum we can assess the achievable noise limited resolution

(a)

(b)
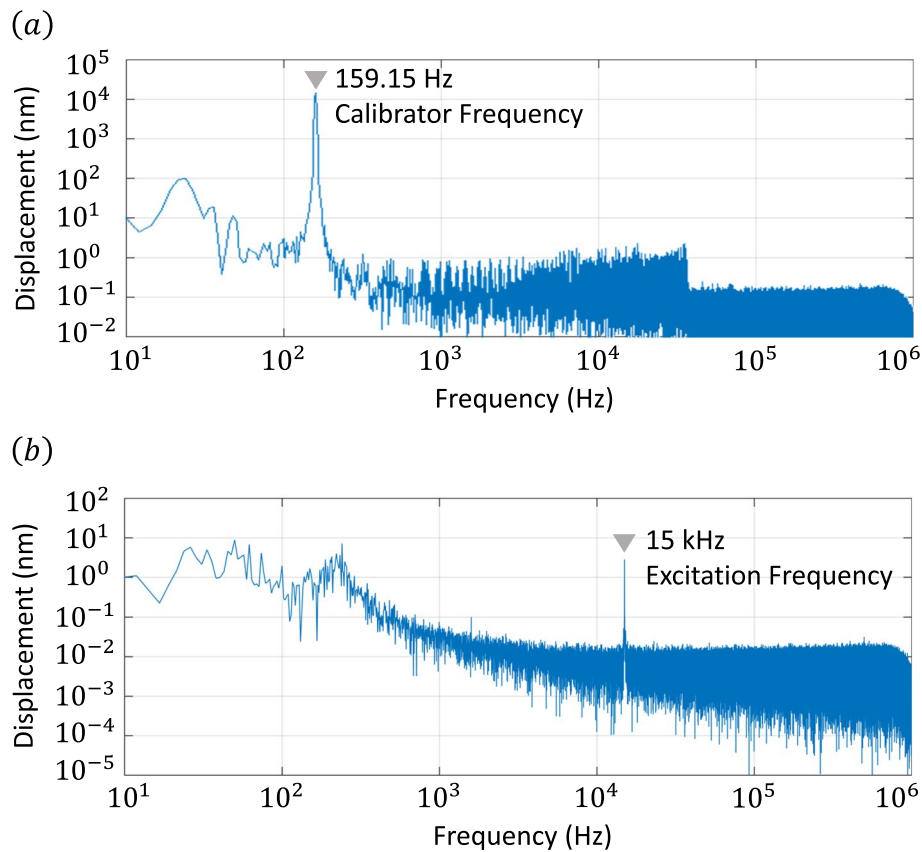
Fig. 15 (Top) Spectrum from the calibration measurement with a sinusoidal vibration frequency at
159.15 Hz with a peak-to-peak displacement amplitude of 14.142 μm. (Bottom) Displacement spectrum
from a loudspeaker using a sinusoidal excitation signal at 15 kHz. Bandpass filtering is applied to improve the
resolution of the measurement (achievable noise floor around 10 pm/√Hz)

of the setup. For frequencies above 1 kHz the noise spectrum is white, and the base line
lies in the range of 10 pm, while for lower frequencies, bellow 200 Hz, the noise level
limits the resolution to a few nm (< 10 nm). The higher noise level at lower frequencies is
primarily due to electronic noise from the circuits used for the detection and digitization
of the signal, while it is also related to vibrations of the environment. The demodulation
of the signal in the above measurements was performed in an offline manner.

Real-time demodulation of the LDV signal is extremely useful, especially in situations
where adjustments in the LDV system or in the measured object are needed in situ.
We conducted measurements on the loudspeaker using real-time demodulation where
the two channels from the two orthogonal polarizations were recorded and analyzed.
Figure 16 shows the displacement spectrum of the measured signals for the two chan-
nels. The observation window was limited to 20 kHz due to the available memory for
the real-time processing. As both polarization channels carry the same information,
the same peak amplitude of 5 nm and the 10 kHz frequency of the moving loudspeaker
membrane is retrieved. The achievable resolution of our measurement is approximately
10 pm. For comparison, a summary of the present work is presented in Table 1 along
with comparable integrated heterodyne sensors based on serrodyne, acousto-optic and
SSB modulation.
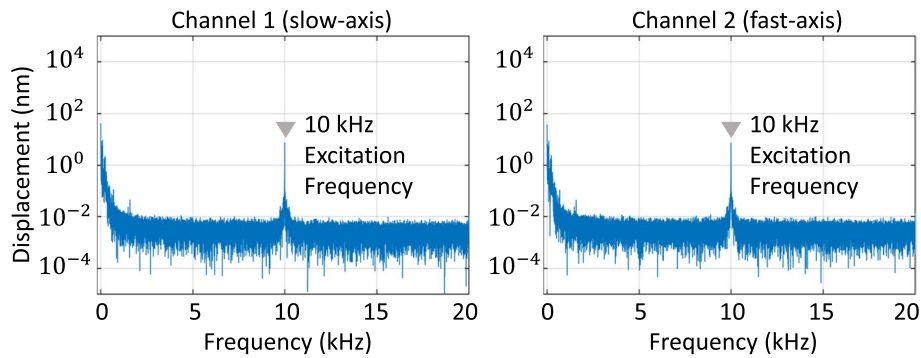
Fig. 16 Displacement spectrum from a loudspeaker using 10 kHz excitation. The two channels correspond to the two independent polarization channels and carry the same information. The achievable displacement resolution is below 10 pm

Table 1 Summary of this work with comparable heterodyne sensors

Year /Author	Platform /Wavelength	OFS (Modulation)	f_{OFS}	Resolution	On-chip detection
1991 [6] /Toda	LiNbO3 /630 nm	Serrodyne (EO)	200 kHz	3 nm	No
2001 [21] /Rubiyanto	LiNbO3 /1561 nm	Acousto-optic (SAW)	171 MHz	105 pm	No
2013 [8] /Li	SOI /1550 nm	Serrodyne (TO)	2 kHz	< 1 nm	No
2015 [9] /Cole	SOI /1550 nm	SSB (TO)	50 Hz	2 nm	Yes (Ge-PDs)
This work	**SiN, Polymer /1550 nm**	**Serrodyne SSB (SO)**	**100 kHz 2.5 MHz**	**10 pm**	**Yes (InP-PDs)**

EO Electro-optic, *TO* Thermo-optic, *SO* Stress-optic

Conclusions

Stress-optic phase modulation in TriPleX is based on the piezoelectric actuation of a PZT layer deposited above the waveguide structures. The actuation is achieved via an electric field applied between two electrodes. In this work we have demonstrated for the first time a top-top electrode configuration in the TriPleX platform, where both electrodes are placed on top of the PZT layer and apply a horizontal electric field through the latter. With the best performing modulator structure, we have reported a 0.25 π peak-to-peak sinusoidal phase-shift at 2.5 MHz with 156 mW power dissipation, while the average power consumption of all fabricated structures was 660 mW. The stress-optic modulators of this work require relative long electrode lengths (15 mm) and high voltage driving signals (> 100 Vpp), rendering them non-competitive with modulators in other material systems (such as LiNbO$_3$ and InP). However, the realization of modulators with a wafer-level process in the silicon nitride platform, capable of operating in the MHz-range is an achievement and can potentially benefit numerous applications that require multiple modulators inside large optical circuits, such as multi-channel sensors or microwave photonics. Further improvement of the modulation efficiency is possible with optimization of the stress distribution in the waveguide. This can be realized by optimizing the dome and electrode structures. Higher modulation and, consequently,

power efficiency is also possible with further improvements in the PZT material quality, in terms of crystal uniformity and piezoelectric efficiency. Moreover, an advantage of the top-top over the conventional top–bottom electrode configuration is the possibility to increase the thickness of the PZT layer without altering the electric field density through the PZT. Thus, the PZT thickness can be further increased and optimized independently to achieve higher efficiency of the stress-optic effect.

We have demonstrated the feasibility of high-quality OFS in the MHz regime, of an optical carrier at 1550 nm, using stress-optic phase modulation in the SiN-based Tri-PleX platform. We have investigated via simulations the performance of the serrodyne and the SSB OFS, and we have presented their limitations in terms of CE and suppression ratio of the unwanted sidebands (SBSR) in practical implementations. Both the serrodyne and the SSB OFSs have been realized in the TriPleX platform and evaluated experimentally, demonstrating frequency shifts at 100 kHz and 2.5 MHz, and SBSR of 22.1 dB and 39 dB, respectively. A key benefit of using TriPleX for the implementation of the OFS units is the potential for high optical power handling that silicon nitride offers, unlike silicon platform that is limited due to two photon absorption [55]. We have integrated the SSB-OFS in a miniaturized LDV system operating at 1550 nm wavelength and demonstrated vibration measurements up to 15 kHz, with the possibility of measuring vibration frequencies up to 1 MHz with 10 pm displacement resolution. Signal detection has been based on a dual-pol coherent receiver realized in the PolyBoard platform utilizing InP-based PDs. In this work, the TriPleX and the PolyBoard PICs have been packaged individually and connected via fiber arrays, to demonstrate the proof-of-concept. A more compact system is possible via hybrid integration of the two units, while we have also reported a powerful 3D integration method for the combination of the TriPleX and the Polyboard platform on a wafer-level [56]. Moreover, hybrid integrated semiconductor laser sources with extremely narrow spectral linewidth are available in the TriPleX platform [57], offering the possibility for on-chip light generation.

We have demonstrated that the stress-optic modulators of the current work can be successfully integrated in a fully functional LDV system that allows the measurement of vibration frequencies at least two orders of magnitude higher from what is possible with the conventional thermo-optic phase shifters of the TriPleX platform. The realization of efficient OFS functionality in the silicon nitride platform with a wafer-scale process is a significant achievement, as it can open the way to the combination of heterodyne interferometric principles and solid-state scanning units (such as OPAs) through monolithic integration, enabling low-cost and compact sensor systems.

Abbreviations

CE	Conversion efficiency
CW	Continuous wave
DRIE	Deep reactive ion etching
DSP	Digital signal processing
EBL	E-beam lithography
ESA	Electrical spectrum analyzer
FPGA	Field programmable gate array
HWP	Half-wave plate
IDT	Inter-digital transducer
LDV	Laser Doppler Vibrometer
LO	Local oscillator
MEMS	Micro-electromechanical system
MMI	Multimode interference

MZM	Mach-Zehnder modulator
OFS	Optical frequency shifter
PBS	Polarization beam splitter
PC	Polarization controller
PD	Photodiode
PH	Phase heater
PIC	Photonic integrated circuit
PLD	Pulsed Laser Deposition
SAW	Surface acoustic wave
SBSR	Sideband suppression ratio
SMSR	Sidemode suppression ratio
SOH	Silicon organic hybrid
SOI	Silicon-on-insulator
SOM	Stress-optic modulator
SSB	Single-sideband
VOA	Variable optical attenuator

Availability of data and materials
All data generated or analyzed during this study are included in this published article.

Declarations

Ethics approval and consent to participate
Not applicable (No human participants or data or tissue).

Consent for publication
Not applicable (No individual person's data are included in any form in this manuscript).

Competing interests
The authors declare that they have no competing interests.

References
1. Rothberg SJ, et al. An international review of laser Doppler vibrometry: Making light work of vibration measurement. Opt Lasers Eng. 2017;99:11–22. https://doi.org/10.1016/j.optlaseng.2016.10.023.
2. Yang J, Yang T, Wang Z, Jia D, Ge C. A novel method of measuring instantaneous frequency of an ultrafast frequency modulated continuous-wave laser. Sensors. 2020;20(14):3834. https://doi.org/10.3390/s20143834.
3. Rogers C, et al. A universal 3D imaging sensor on a silicon photonics platform. Nature. 2021;590(7845):256–61. https://doi.org/10.1038/s41586-021-03259-y.
4. Park Y, Cho K. Heterodyne interferometer scheme using a double pass in an acousto-optic modulator. Opt Lett. 2011;36(3):331. https://doi.org/10.1364/OL.36.000331.
5. Mychkovsky AG, Chang NA, Ceccio SL. Bragg cell laser intensity modulation: effect on laser Doppler velocimetry measurements. Appl Opt. 2009;48(18):3468. https://doi.org/10.1364/AO.48.003468.
6. Toda H, Haruna M, Nishihara H. Integrated-optic heterodyne interferometer for displacement measurement. J Lightwave Technol. 1991;9(5):683–7. https://doi.org/10.1109/50.79546.

7.   Li Y, Meersman S, Baets R. Optical frequency shifter on SOI using thermo-optic serrodyne modulation. In 7th IEEE International Conference on Group IV Photonics. Beijing: IEEE; 2010. p. 75–77. https://doi.org/10.1109/GROUP4.2010.5643423.

8.   Li Y, et al. Heterodyne laser Doppler vibrometers integrated on silicon-on-insulator based on serrodyne thermo-optic frequency shifters. Appl Opt. 2013;52(10):2145. https://doi.org/10.1364/AO.52.002145.

9.   Cole DB, Sorace-Agaskar C, Moresco M, Leake G, Coolbaugh D, Watts MR. Integrated heterodyne interferometer with on-chip modulators and detectors. Opt Lett. 2015;40(13):3097. https://doi.org/10.1364/OL.40.003097.

10. Li Y, Dieussaert E, Baets R. Miniaturization of laser doppler vibrometers—a review. Sensors. 2022;22(13):4735. https://doi.org/10.3390/s22134735.

11. Izutsu M, Shikama S, Sueta T. Integrated optical SSB modulator/frequency shifter. IEEE J Quantum Electron. 1981;17(11):2225–7. https://doi.org/10.1109/JQE.1981.1070678.

12. Shimotsu S, et al. Single side-band modulation performance of a LiNbO 3 integrated modulator consisting of four-phase modulator waveguides. IEEE Photonics Technol Lett. 2001;13(4):364–6. https://doi.org/10.1109/68.917854.

13. Yamazaki H, Saida T, Goh T, Mori A, Mino S. Dual-carrier IQ modulator with a complementary frequency shifter. Opt Express. 2011;19(26):B69. https://doi.org/10.1364/OE.19.000B69.

14. Kodigala A, et al. Silicon Photonic Single-Sideband Generation with Dual-Parallel Mach-Zehnder Modulators. In Conference on Lasers and Electro-Optics. San Jose, California; 2019. https://doi.org/10.1364/CLEO_SI.2019.STh4N.6.

15. Hasan GM, Hasan M, Hall TJ. Performance analysis of a multi-function mach-zehnder interferometer based photonic architecture on SOI acting as a frequency shifter. Photonics. 2021;8(12):561. https://doi.org/10.3390/photonics8120561.

16. Alexander K, et al. Nanophotonic Pockels modulators on a silicon nitride platform. Nat Commun. 2018;9(1):3444. https://doi.org/10.1038/s41467-018-05846-6.

17. Lauermann M, et al. Integrated optical frequency shifter in silicon-organic hybrid (SOH) technology. Opt Express. 2016;24(11):11694. https://doi.org/10.1364/OE.24.011694.

18. Reed GT, et al. Recent breakthroughs in carrier depletion based silicon optical modulators. Nanophotonics. 2014;3(4–5):229–45. https://doi.org/10.1515/nanoph-2013-0016.

19. Spuesens T, et al. Integrated Optical Frequency Shifter on a Silicon Platform. In Conference on Lasers and Electro-Optics. San Jose, California; 2016. https://doi.org/10.1364/CLEO_SI.2016.SF2G.1.

20. Yamaguchi Y, Kanno A, Kawanishi T, Izutsu M, Nakajima H. Pure Single-Sideband Modulation Using High Extinction-Ratio Parallel Mach-Zehnder Modulator with Third-Order Harmonics Superposition Technique. In CLEO: 2015. San Jose, California: 2015. p. JTh2A.40. https://doi.org/10.1364/CLEO_AT.2015.JTh2A.40.

21. Rubiyanto A, Herrmann H, Ricken R, Tian F, Sohler W. Integrated optical heterodyne interferometer in lithium nio-bate. J Nonlinear Optic Phys Mat. 2001;10(02):163–8. https://doi.org/10.1142/S0218863501000516.

22. Edinger P, et al. Silicon photonic microelectromechanical phase shifters for scalable programmable photonics. Opt Lett. 2021;46(22):5671. https://doi.org/10.1364/OL.436288.

23. Jin W, Polcawich RG, Morton PA, Bowers JE. Piezoelectrically tuned silicon nitride ring resonator. 2018:14.

24. Huang M. Stress effects on the performance of optical waveguides. Int J Solids Struct. 2003;40(7):1615–32. https://doi.org/10.1016/S0020-7683(03)00037-4.

25. Donati S, Barbieri L, Martini G. Piezoelectric actuation of silica-on-silicon waveguide devices. IEEE Photon Technol Lett. 1998;10(10):1428–30. https://doi.org/10.1109/68.720283.

26. Tsia KK, Fathpour S, Jalali B. Electrical tuning of birefringence in silicon waveguides. Appl Phys Lett. 2008;92(6):061109. https://doi.org/10.1063/1.2883925.

27. Sebbag Y, et al. Bistability in silicon microring resonator based on strain induced by a piezoelectric lead zirconate titanate thin film. Appl Phys Lett. 2012;100(14):141107. https://doi.org/10.1063/1.3701587.

28. Schriever C, Bohley C, Schilling J, Wehrspohn RB. Strained silicon photonics. Materials. 2012;5(12):889–908. https://doi.org/10.3390/ma5050889.

29. Hosseini N, et al. Stress-optic modulator in TriPleX platform using a piezoelectric lead zirconate titanate (PZT) thin film. Opt Express. 2015;23(11):14018. https://doi.org/10.1364/OE.23.014018.

30. Epping JP, et al. Ultra-low-power stress-optics modulator for microwave photonics. Presented at the SPIE OPTO. San Francisco, California: 2017. 101060F. https://doi.org/10.1117/12.2266170.

31. Epping JP, et al. Ultra-low-power stress-based integrated photonic phase actuator. 2018:3.

32. Everhardt A, et al. Ultra-low power stress-based phase actuation in TriPleX photonic circuits. In Integrated Optics: Devices, Materials, and Technologies XXVI. San Francisco: 2022. p. 11. https://doi.org/10.1117/12.2609405.

33. Casset F, et al. Stress optic modulator using thin-film PZT for LIDAR applications. In 2019 IEEE SENSORS, Montreal: IEEE; 2019. p 1–4. https://doi.org/10.1109/SENSORS43011.2019.8956537.

34. Wang J, Liu K, Harrington MW, Rudy RQ, Blumenthal DJ. Silicon nitride stress-optic microresonator modulator for optical control applications. Opt Express. 2022;30(18):31816. https://doi.org/10.1364/OE.467721.

35. van der Slot PJM, Porcel MAG, Boller K-J. Surface acoustic waves for acousto-optic modulation in buried silicon nitride waveguides. Opt Express. 2019;27(2):1433. https://doi.org/10.1364/OE.27.001433.

36. Ansari I, et al. Light modulation in Silicon photonics by PZT actuated acoustic waves. ArXiv211207988 Phys. 2021. Accessed 30 Jan 2022. Available: http://arxiv.org/abs/2112.07988

37. Tsokos C, et al. True time delay optical beamforming network based on hybrid inp-silicon nitride integration. J Lightwave Technol. 2021;39(18):5845–54. https://doi.org/10.1109/JLT.2021.3089881.

38. Nguyen MD, Tiggelaar R, Aukes T, Rijnders G, Roelof G. Wafer-scale growth of highly textured piezoelectric thin films by pulsed laser deposition for micro-scale sensors and actuators. J Phys Conf Ser. 2017;922:012022. https://doi.org/10.1088/1742-6596/922/1/012022.

39. Nguyen MD, Houwman EP, Dekkers M, Rijnders G. Strongly enhanced piezoelectric response in lead zirconate titan-ate films with vertically aligned columnar grains. ACS Appl Mater Interfaces. 2017;9(11):9849–61. https://doi.org/10.1021/acsami.6b16470.

40. de Felipe D, et al. Recent developments in polymer-based photonic components for disruptive capacity upgrade in data centers. J Light Technol. 2017;35(4):683–9. https://doi.org/10.1109/JLT.2016.2611240.

41. Zhang Z, et al. Hybrid photonic integration on a polymer platform. MDPI Photonics. 2015;2(3):1005–26.
42. Katopodis V, et al. Multi-flow transmitter based on polarization and optical carrier management on optical polymers. IEEE Photonics Technol Lett. 2016;28(11):1169–72.
43. Katopodis V, et al. Polymer enabled 100 Gbaud connectivity for datacom applications. Elsevier Optics Commun. 2016;362:13–21.
44. Johansmann M, Siegmund G, Pineda M. Targeting the Limits of Laser Doppler Vibrometry. 2005.
45. Siegmund G. Sources of measurement error in laser Doppler vibrometers and proposal for unified specifications. Presented at the Eighth International Conference on Vibration Measurements by Laser Techniques. Ancona: Advances and Applications; 2008. 70980Y. https://doi.org/10.1117/12.803150.
46. Li Y, Meersman S, Baets R. Realization of fiber-based laser Doppler vibrometer with serrodyne frequency shifting. Appl Opt. 2011;50(17):2809. https://doi.org/10.1364/AO.50.002809.
47. Johnson LM, Cox CH. Serrodyne optical frequency translation with high sideband suppression. J Light Technol. 1988;6(1):109–12. https://doi.org/10.1109/50.3974.
48. Roeloffzen CGH, et al. Low-loss Si3N4 TriPleX optical waveguides: technology and applications overview. IEEE J Sel Top Quantum Electron. 2018;24(4):1–21. https://doi.org/10.1109/JSTQE.2018.2793945.
49. Solmates B.V., website: http://www.solmates-pld.com
50. Blank DHA, Dekkers M, Rijnders G. Pulsed laser deposition in Twente: from research tool towards industrial deposition. J Phys Appl Phys. 2014;47(3);034006. https://doi.org/10.1088/0022-3727/47/3/034006.
51. Kleinert M, et al. Photonic integrated devices and functions on hybrid polymer platform. Presented at the SPIE OPTO. San Francisco, California; 2017. p. 100981A. https://doi.org/10.1117/12.2256987.
52. Maese-Novo A, et al. Thermally optimized variable optical attenuators on a polymer platform. Appl Opt. 2015;54(3):569. https://doi.org/10.1364/AO.54.000569.
53. Polytec GmbH., website: https://www.polytec.com/
54. Dekkers M, et al. The significance of the piezoelectric coefficient $d_{31,\text{eff}}$ determined from cantilever structures. J Micromechanics Microengineering. 2013;23(2):025008. https://doi.org/10.1088/0960-1317/23/2/025008.
55. Shekhar S, et al. Silicon Photonics - Roadmapping the Next Generation. 2023.
56. Raptakis A, et al. Fully integrated Laser Doppler Vibrometer (LDV) based on hybrid 3D integration of silicon nitride and polymer photonic circuits with operation in the kHz regime. In Garcia-Blanco SM, Cheben P, editors. Integrated Optics: Devices, Materials, and Technologies XXVII. San Francisco: SPIE; 2023. p. 15. https://doi.org/10.1117/12.2650027.
57. Boller K-J, et al. Hybrid Integrated Semiconductor Lasers with Silicon Nitride Feedback Circuits. Photonics. 2019;7(1):4. https://doi.org/10.3390/photonics7010004.

Publisher's Note